Promoting reversible anionic redox in sodium-ion cathodes by doping and phase control

Shipeng Jia[1], Marzieh Abdolhosseini[1], Yixuan Li[1], Sang-Jun Lee[2], Hirohito Ogasawara[2], Ning Chen[3], Alex Hebert[1], J. Michael Sieffert[1], Maddison Eisnor[1], and Eric McCalla[1,*]

1. Department of Chemistry, McGill University, Montreal, QC, Canada

2. Stanford Synchrotron Radiation Lightsource, SLAC National Accelerator Laboratory, Menlo Park, CA, USA

3. Science Division, Canadian Light Source Inc., 44 Innovation Boulevard, Saskatoon, SK, S7N 2V3, Canada

* Corresponding author: eric.mccalla@mcgill.ca

Abstract:

Important efforts are underway to harness anionic redox to obtain high energy Na-ion cathodes. Previously, we identified disruptive dopants in Na-Mn-O that induced reversible oxygen redox. Here, we perform detailed mechanistic studies to understand why they are effective. First, we confirm that no transition metals are being oxidized, it is indeed oxygen redox. We also identify that reversible transition metal migration occurs in the P2 phase where reversible anionic redox occurs, while the migration is irreversible in the distorted P'2 phase. Structural control over the anionic redox is highly significant, but we further elucidate the role of the disruptive dopants. Localized oxygen holes are identified as the source of the reversible anionic redox and these are deemed to remain stable due to the dopants minimizing the interactions between oxygens to prevent their dimerization. These important contributions to understand anionic redox will help realize viable high energy Na-ion batteries.

1. Introduction

Due to the depletion of non-renewable fossil fuels and the increasing global energy demand, there has been a significant shift towards electrification, with traditional internal combustion engines being replaced by more energy-efficient and environmentally friendly electric vehicles.[1] This transition has driven a rapidly growing demand for sustainable energy storage technologies, with lithium-ion batteries (LIBs) dominating the market over the past decade.[2–4] To address the pressing need for sustainability and effective cost, sodium-ion batteries (SIBs) have emerged as a promising next-generation alternative to LIBs.[5–7] Leveraging the abundant availability of sodium resources and cost-effective production potential, SIBs offer a more environmentally and economically sustainable solution for future energy storage applications. However, despite their potential, achieving competitive electrochemical performance in SIBs—particularly in terms of energy density and operating voltage—remains a critical challenge.[8,9] Conventional cathode materials are primarily limited to redox contributions from transition metals (TMs), creating an upper limit on specific capacity and thus energy density. Overcoming this limitation is essential to unlock the full potential of SIBs as viable contenders for large-scale energy storage and electrification solutions.

One promising approach to overcoming the limitations of sodium-ion batteries involves leveraging anionic redox mechanisms.[10] Oxygen redox, in particular, has shown great potential to unlock additional capacity beyond the conventional cationic redox processes. Despite its promise, the practical realization of reversible oxygen redox remains challenging. Current research primarily focuses on limited classes of materials, such as lithium-doped oxides like $NaLi_{1/3}Mn_{2/3}O_2$[11] or sodium-rich layered oxides like Na_2IrO_3[12] and Na_2RuO_3[13]. The core design strategy centers on elevating the energy of the non-bonding orbitals of lattice oxygen, so they lie at the Fermi energy, E_f, and thereby participate in the redox processes at high voltages.[14] By introducing monovalent ions such as Li^+ or Na^+ into the transition metal sites, traditionally occupied by multivalent *nd*-orbitals, localized distortions are created to activate the energy level of the antibonding s^* orbital from O-O bond.[15–17] These distortions alter the hybridization between transition metals and oxygen (TM–O), potentially stabilizing the $(O\text{-}O)^{n-}$ species and promote oxygen redox activity. However, there is the risk that the O-O distance shortens as further oxidation occurs, leading to the irreversible release of O_2 gas associated with capacity loss, and structural collapse.[18]

Quantifying oxygen redox contributions is challenging and often requires advanced synchrotron-based X-ray techniques, such as X-ray absorption spectroscopy (XAS)[19] and resonant inelastic X-ray scattering (RIXS)[20]. In our previous study[21], we conducted high-throughput investigations[22–25] involving 52 different dopants in the earth-abundant and environmentally friendly cathode system $Na_{0.67}Mn_{0.9}X_{0.1}O_2$, where X represents the dopants. A key finding was that several doped cathodes demonstrated high-voltage redox activity, which we attributed to oxygen redox, though the materials were mixtures of the P2 and P'2 phases which raises doubts about which phase shows active oxygen. Notably, the undoped $Na_{0.67}MnO_2$ material did not exhibit any high-voltage activity above 4.0 V. Herein, we identify the P2 phase as being the structure where reversible anionic redox occurs, but we must emphasize that our past work clearly shows that having the P2 structure is not sufficient to ensure oxygen redox, in fact 3 pure P2 materials (Li, Mg and Fe doped) showed no anionic redox whatsoever in ref. [21]. The role of the dopants in inducing oxygen redox was further correlated the bond valence mismatch (BVM) calculated for the various dopants.[21] Our results indicated that a larger mismatch promotes the ionic character of the bonding with oxygen (more electron density on oxygen), thereby facilitating the oxidation of O 2*p* orbitals. In fact, we have discovered benefits to using large dopants in anodes, cathodes and solid electrolytes.[36] In the current study, we solely select dopants with significant bond valence mismatches—K, Rb, Cs, Cu, and Tl (these all have large BVM and larger radii than Mn as shown in Table S1, but only Cu and Tl have large electronegativities)—to incorporate into $Na_{0.67}Mn_{0.9}X_{0.1}O_2$ and we prepare these as either pure P2 or P'2 phases. This approach therefore aims to both further elucidate the mechanisms underpinning the oxygen redox activity.

2. Results and Discussion

The X-ray diffraction (XRD) patterns shown in Figure 1 confirm the successful synthesis of the P2 and P'2 samples through doping and phase control as detailed in the methods section. Both the P2 and P'2 samples were synthesized using the same sol-gel procedure and sintered at 850°C for 12 hours, but by then quenching from either 450°C or 600°C, the pure P2 and P'2 phases were obtained, respectively. As will be seen below, only the P2 materials show reversible oxygen redox. Thus, careful comparison of the two structures is essential, so we performed Rietveld refinements on all structures using the *Cmcm* space group only to allow direct comparison of the structures. The results are summarized in Tables S2 and S3 and discussed in detail in the SI section "Further structural discussion". Importantly, all P'2 structures show enlarged Na slabs (i.e. the oxygens

above and below the Na are further apart in the prismatic sites), and much of this is attributed to a higher dopant concentration in the Na layer in the P'2 structures (hindering O repulsion). It is also important to recognize that Jahn-Teller distortions are not the only factor impacting the nature of the octahedra on the TM layer, and large dopants like Cs and Rb end up distorting the octahedra more than the Jahn-Teller effect.

Furthermore, thermogravimetric analysis (TGA), as shown in Figure S2, highlights the critical role of the cooling process. Upon cooling from 850°C to 600°C, there is negligible mass change, while a small but significant mass gain is seen between 600 and 450 °C which corresponds to oxygen uptake. Thus, the P'2 material made by quenching from 600°C is oxygen deficient, which is compensated for with Mn^{3+} that is Jahn-Teller active and induces lattice strain. By contrast, the oxygen uptake down to 450°C results in the oxidation of Mn^{3+} to Mn^{4+}, effectively suppressing Jahn-Teller distortion and giving the undistorted P2 hexagonal structure, as evidenced by Table S3, where the lattice *b/a* ratio equals to √3.

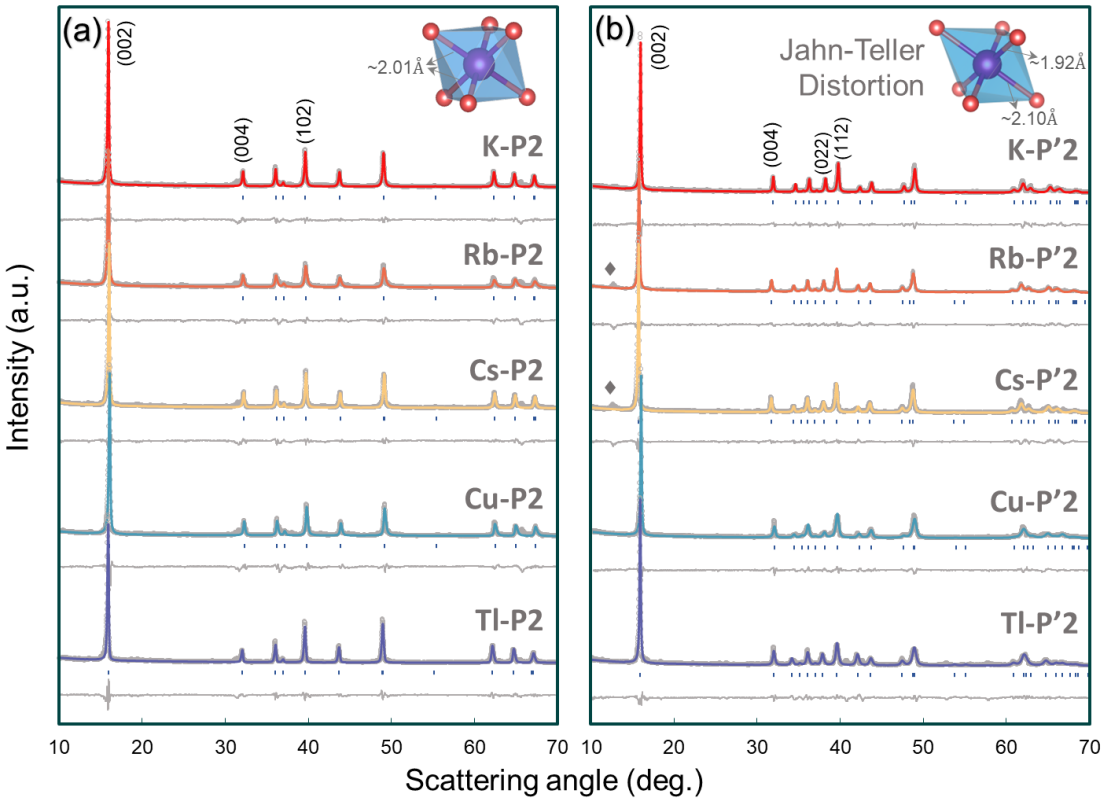

Figure 1: X-ray diffraction patterns of doped samples exhibiting (a) the P2 structure and (b) the P'2 structure, where the prime symbol (') denotes the Jahn-Teller distortion induced by Mn^{3+}. The

insets illustrate the transition metal coordination environments and corresponding bond lengths for undoped materials (the corresponding values for the 10 materials reported here are in Table S3 and they differ significantly from these, particularly for the large dopants like Rb and Cs).

The structural differences lead to striking variations in electrochemical behavior, as shown in Figure 2. The cyclic voltammetry (CV) curves of the P2 materials reveal smoother charge and discharge profiles compared to the P'2 materials, where multiple redox peaks are observed. Notably, the high-voltage behavior (>4.0 V) of the two phases differs completely: all P2 materials exhibit reversible high-voltage redox processes, whereas P'2 materials all show an irreversible oxidation process. As previously mentioned, bond valence mismatches can serve as indicators of anionic redox activity.[21] In particular, Cs- and Tl-doped samples demonstrate stronger oxygen redox activity. The exception to this is Cu, which has a more moderate bond valence mismatch, however, it shows the strongest reversible high voltage peak. We speculate that this is due to nearly all of the Cu occupying the TM layer, whereas all other dopants show less occupation on the TM layer (Table S3), however, it is possible that Cu's highest electronegativity (Table S1) also contributes by increasing the ionic character of the M-O bonds. There is thus an optimal dopant that is both large enough to induce the anionic redox but small enough to still occupy the TM layer; and we also recognize that dopants with a higher electronegativity (see Table S1) like Tl and Cu do not require as large a BVM to induce the oxygen redox. Two prominent pairs of high-voltage peaks were observed across all five doped P2 materials, located at approximately 4.27 V/4.12 V and 4.59 V/4.52 V. Remarkably, unlike the significant voltage hysteresis commonly observed in Li-rich cathodes (>1.0 V)[15,26,27], the overpotentials for these two pairs are notably small, measuring around 0.15 V and 0.07 V, respectively. These peaks are also not kinetically hindered (peak values of 15 mA/g and higher); in Li-rich cathodes we achieve much smaller currents and in fact CVs must be performed at very slow rates to see the anionic redox[28]. This minimal hysteresis and rapid kinetics underscores the exceptional reversibility of the oxygen redox processes in these novel materials.

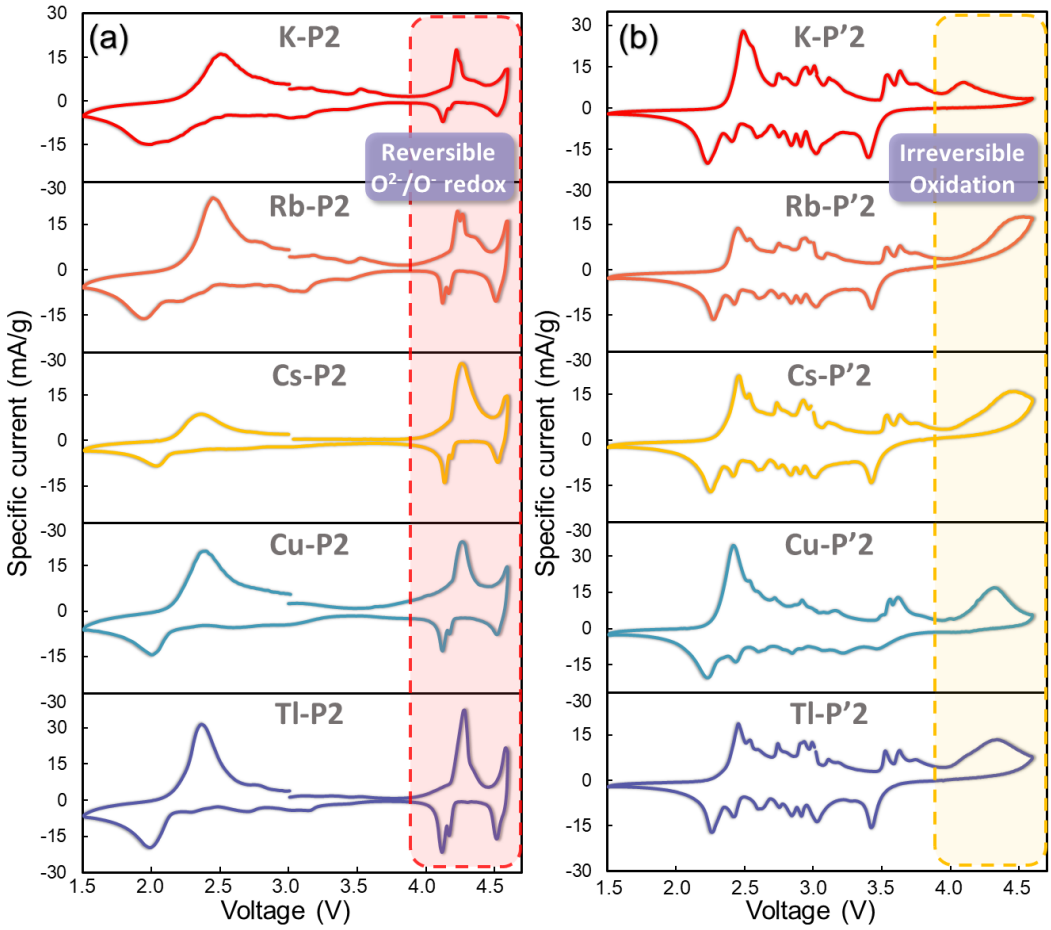

Figure 2: Cyclic voltammetry (CV) curves for the first cycle of all doped samples in (a) the P2 phase and (b) the P'2 phase, measured within the voltage range of 1.5 V to 4.6 V at a scan rate of 0.1 V h^{-1}. The P2 materials exhibit reversible redox peaks in the high-voltage region (>4.0 V), whereas the P′2 materials display irreversible oxidation at high voltages. The oxygen redox in the Rb-P2 material near 4.2 V shows a doublet indicating that a phase transition may be taking place. All other P2 materials show a single peak in this region only.

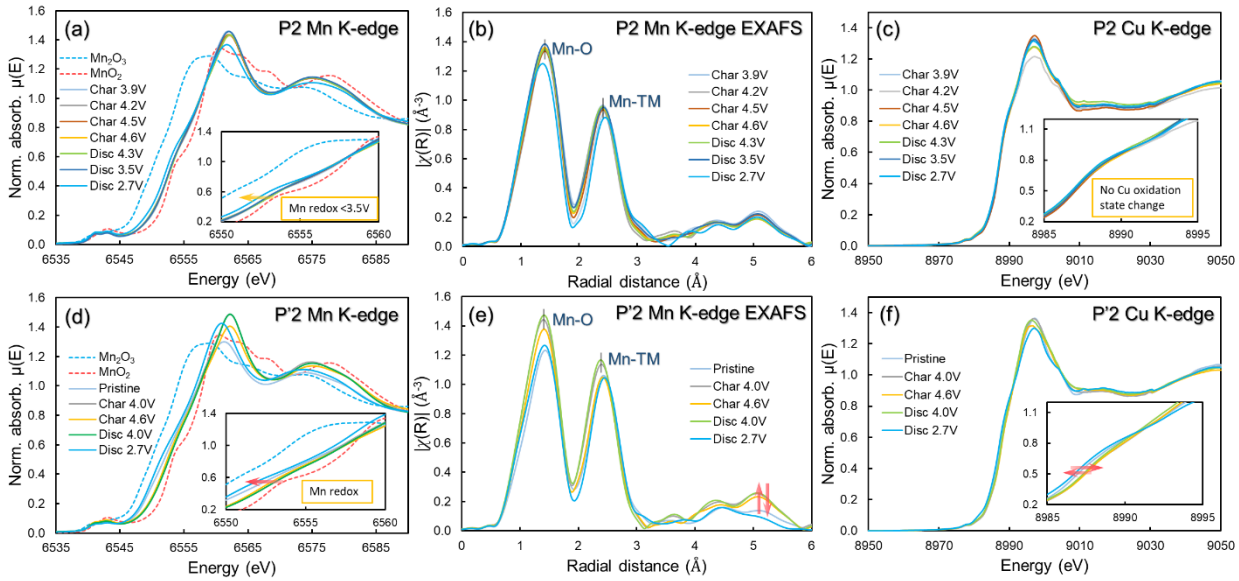

Figure 3: X-ray absorption spectroscopy (XAS) analysis comparing Cu-doped P2 and P'2 *ex-situ* cathodes. (a, d) XANES spectra at the Mn K-edge for P2 and P'2, respectively. (b, e) Fourier-transformed EXAFS at the Mn K-edge for P2 and P'2, respectively. (c, f) XANES spectra at the Cu K-edge for P2 and P'2.

To ensure that the high voltage peaks are in fact anionic redox and not due to TM redox, we conducted a comprehensive analysis of over 80 X-ray absorption spectra (XAS) from *ex-situ* cathodes, as summarized in Figures 3, S3–S7. In Figures 3a, S3-S6, the X-ray Absorption Near-Edge Structure (XANES) spectra for the Mn K-edge of all P2 material show Mn is close to 4+ with no further oxidation during charge. A shift toward lower energy is observed only below 3.5 V, aligning with the Mn^{3+}/Mn^{4+} redox process, which predominantly occurs below 3.0 V, as shown in Figure 2a. Additionally, the XANES spectra for the Cu K-edge (Figure 3c) do not manifest any edge shift, confirming that Cu does not participate in charge compensation. By contrast, all P'2 materials exhibit Mn K-edge XANES spectra showing that pristine materials have Mn with oxidation states well below 4. These results are consistent with the CV curves in Figure 2b, which demonstrate the more intricate electrochemical behavior of P'2 materials where Mn^{3+} is oxidized during charge. Furthermore, Extended X-ray Absorption Fine Structure (EXAFS) analysis reveals greater local structural changes in the P'2 material (Figure 3e) compared to the P2 material (Figure 3b). The XANES spectra for the Cu K-edge in P'2 materials also show a slight shift toward higher energy, potentially indicating a Cu^{2+}/Cu^{3+} oxidation process, as previously reported in the literature[29–31].

To further quantify structural variations, we systematically compared the Fourier-transformed EXAFS (FT-EXAFS) peaks, with results summarized in Tables S4 and S5 for P2 and P'2 samples, respectively. The P2 materials exhibit overall smaller structural variations and superior structural reversibility compared to the P'2 materials. For example, the average change in the first-shell Mn-O intensity between the fully charged (4.6 V) and pristine samples is only 5.4% for P2 samples, while it is 20.4% for P'2 samples—a nearly fourfold difference. This significant disparity in structural modification likely explains the differences in oxygen redox reversibility. Specifically, the stability of the local Mn-O hybridization is key to modulating the energy level of oxygen's non-bonding 2*p* orbitals[32]. Additionally, dopants were found to have a substantial impact on structural stability. Notably, Cu- and Rb-doped samples demonstrate better structural stability, consistent across both P2 and P'2 phases, as detailed in Tables S4 and S5.

To further elucidate the mechanism of oxygen redox, we employed Resonant Inelastic X-ray Scattering (RIXS), a technique that simultaneously collects excitation and emission photon energies to generate a two-dimensional map[20,33]. Due to the long measurement times required, we selected two materials to focus on: the Cu-doped as the most reversible anionic redox material and the Cs-doped material as an example of a very high bond valence mismatch dopant. The RIXS map provides enhanced resolution of the O K-edge features and reveals the hybridization between TM-3*d* and O-2*p* orbitals, as illustrated in Figure 4. Two distinct hot spots are identified in the RIXS maps shown in Figures 4a–c and 4f–h. A prominent hot spot appears at an excitation energy of 529.5 eV, accompanied by a weaker shoulder at approximately 532 eV. The intense hot spot at the lower excitation energy (529.5 eV) corresponds to a superposition of the $t_{2g}\downarrow$ state and the $e_g\uparrow$ state, collectively accommodating five electrons. In contrast, the weaker shoulder at 532 eV is associated with the $e_g\downarrow$ state, which contains the remaining two electrons.[34,35] These observations underscore the sensitivity of the RIXS technique to orbital-specific interactions, making it an invaluable tool for probing the electronic and orbital contributions to the oxygen redox process.

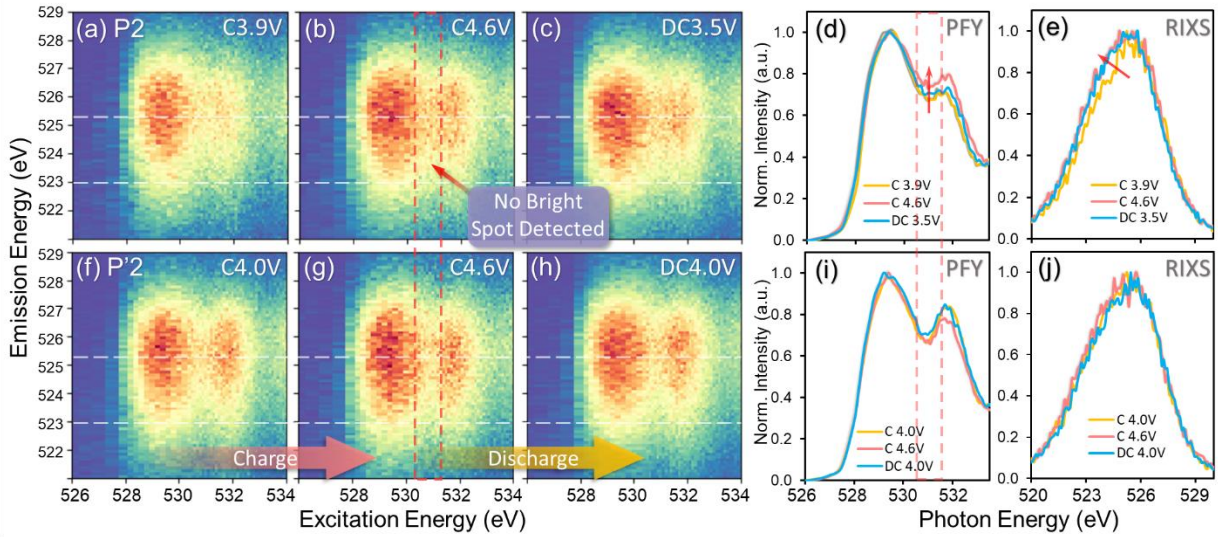

Figure 4: Resonant inelastic X-ray scattering (RIXS) maps of the O K-edge for (a–c) Cu-doped P2 and (f–h) Cu-doped P'2 ex-situ cathodes. (d, i) Partial fluorescence yield (PFY) XAS spectra at the O K-edge for P2 and P′2, respectively. (e, j) Integration of RIXS spectra over the excitation energy range of 530.5–531.5 eV (region bound by red dashed lines in (b, g). The intersection of the red and white guidelines highlights the active region commonly associated in the literature with the formation of dimers or peroxo-like species.

Two common mechanisms are commonly known to stabilize oxidized oxygen species. The first involves the formation of dimers or peroxo-like $(O\text{-}O)^{n-}$ species, characterized by a significant reduction in neighboring oxygen bond lengths (from ~2.86 Å oxides to ~1.49 Å in peroxide).[36] This mechanism has been widely reported in Li-rich cathodes.[37–39] Such dramatic lattice oxygen bond shortening triggers a distinct bright spot in the RIXS map, serving as a fingerprint for the formation of $(O\text{-}O)^{n-}$ species. This feature is typically observed near an excitation photon energy of 531 eV and an emission energy between 523–524 eV[27,37], as indicated by the guide lines in Figure 4b and 4g. However, the RIXS maps for the *ex-situ* cathodes at the fully charged state do not show this feature. Instead, upon integrating the emission and excitation energies, we observe minor changes in the peak profiles of the Partial Fluorescence Yield (PFY)[40] and RIXS spectra. Specifically, there is a subtle increase in peak intensity at an excitation energy of 531 eV (Figure 4d) and an emission energy of 524 eV (Figure 4e). Such features are absent in the P'2 materials, as illustrated in Figures 4i and 4j. Similar changes can also be observed in the Cs-doped samples shown in Figure S11. These subtle shifts in the O K-edge spectra suggest the occurrence of oxygen redox[37,41,42], further supporting the presence of reversible oxygen oxidation in the P2 materials.

Given that only mild changes are observed in the PFY and the absence of the additional hot spot in RIXS maps, the dimer or peroxo $(O\text{-}O)^{n-}$ mechanism appears to not be at play. Instead, the primary contribution to the oxygen redox likely arises from the second mechanism: the formation of localized electron-holes on lattice oxygen[36,43]. In this scenario, the partial oxidation of O^{2-} generates holes in the oxygen 2*p* orbitals. When these holes localize on specific oxygen sites, the minimal changes in the M–O bond intensity observed in Figure 3b suggest that stabilizing the local structures is critical for supporting the localized electron-hole configuration.[44] This mechanism is often associated with TM vacancies, as seen in materials such as $Na_2Mn_3O_7$[40,45]. To further validate this mechanism, we compared the RIXS maps of freshly prepared samples with those stored for six months in an Ar-filled glove box, as shown in Figure S10: they are identical, demonstrating the robustness of the oxidized materials. The consistent spectral features across the storage period highlight the stability of the localized electron-hole configuration. We speculate that large dopants (even Cu and Tl are larger than Mn, see Table S1) play an essential role in stabilizing the localized holes by preventing neighboring oxygens from interacting. Thus, by modulating the local structural environment, dopants can dramatically reinforce the stability of the electron-hole configuration[46], further enhancing the overall performance of the material.

The origin of TM vacancies is also commonly associated with the migration of TMs into the Na layer in the charged material. To investigate this phenomenon, we performed wavelet transform (WT) analysis on the EXAFS spectra of *ex-situ* cathodes[47,48], focusing on the kinetic processes during charge and discharge cycles in doped materials. In Figure 5, the WT-EXAFS data for the Cu-doped P'2 sample reveal that Cu reversibly migrates from the TM layer into the Na layer, with Cu acting as a coordinator to stabilize the vacancy. Notably, the WT-EXAFS analysis of Cu-doped P'2 indicates a loss of long-range ordering, suggesting that Cu migration into the Na layer is accompanied by structural reordering around the TM vacancies. This process appears to result in irreversible oxygen oxidation. For the Cu-doped P2 phase, Figure 5 shows a much more moderate decrease in the intensity of the second-shell Cu-TM interaction upon charging to 4.6 V as compared to the P'2 materials. Subsequently, the Cu ions return to their original positions upon discharging to 3.5 V. Notably, even at 4.6 V, the WT-EXAFS maintains long-range ordering (Figure 5c), indicating that some Cu may migrate into the Na layer but they remain near the TM vacancy rather than further diffusing within the Na layer. This stabilization explains the rapid restoration observed after discharge (Figure 5d). In comparison, the WT-EXAFS of the Mn K-edge for Cu-

doped P2 materials (Figure S13) displays consistent patterns, with both short- and long-range ordering well-preserved throughout the charge-discharge process. This strongly suggests that Cu doping effectively suppresses Mn migration. Importantly, reversible TM migration plays a critical role in maintaining structural integrity.[49] Overall, the WT-EXAFS results reveal the critical role of dopants in stabilizing TM vacancies through reversible migration during high-voltage operation, thereby mitigating structural degradation and enhancing oxygen redox stability.

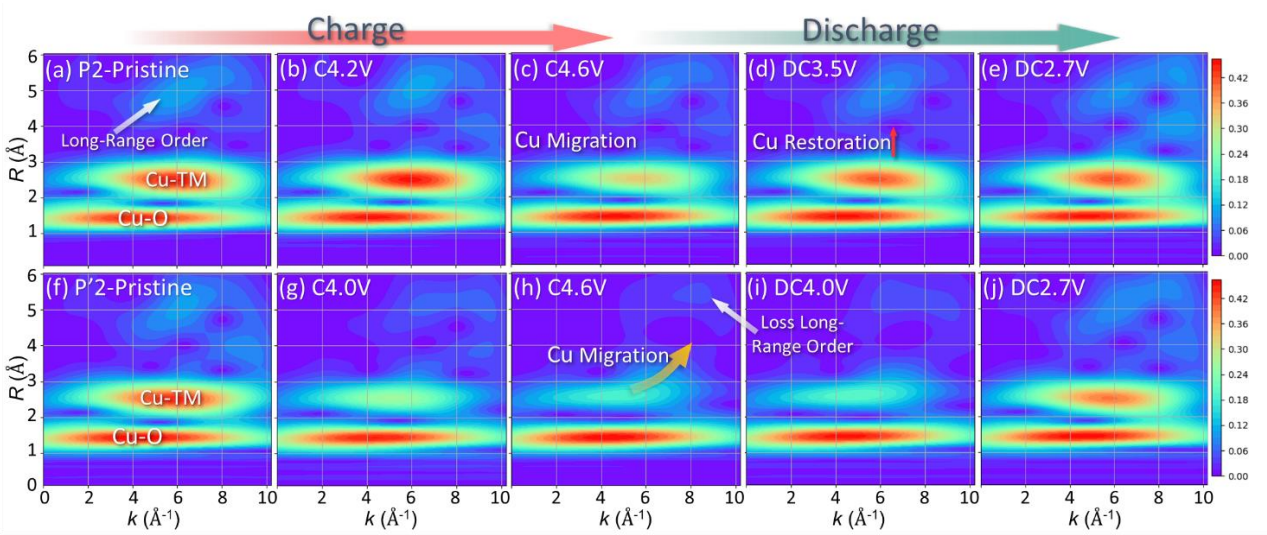

Figure 5: Wavelet transform (WT) of EXAFS at the Cu K-edge for (a–e) Cu-doped P2 and (f–j) Cu-doped P'2 *ex-situ* cathodes. The *k*-*R* space maps illustrate the evolution of electronic structure and bonding distributions during charge and discharge steps. The first coordination shell corresponds to Cu–O bonds, while the second shell is attributed to Cu–TM bonds (primarily Cu–Mn, given the 10% Cu content). The WT-EXAFS plots reveal different structural behaviour in long-range ordering and Cu migration between the P2 and P'2 phases.

3. Conclusion

In this study, a novel design strategy is used to enhance anionic redox activity and stability in layered oxides for sodium-ion batteries by combining selective doping with precise phase control. By leveraging dopants with high bond valence mismatches[21]—such as K, Rb, Cs, Cu, and Tl—we effectively modulated the hybridization of TM-O bonds, enabling the oxidation of non-bonding oxygen 2*p* orbitals at high voltage (>4.0 V). Notably, we identify that it is only the P2 materials that exhibited reversible oxygen redox activity, though the correct dopant choice is also essential. In contrast, the P'2 materials demonstrated only irreversible oxygen redox.

Through comprehensive electrochemical analysis and over 80 *ex-situ* XAS spectra, we elucidated the electronic and structural transformations associated with oxygen redox. The reversible migration of dopants further mitigates phase transitions and structural degradation. Furthermore, RIXS analysis of the P2 samples revealed that the primary mechanism of oxygen redox in the P2 materials stems from localized electron-holes on lattice oxygen, and these show remarkably low overpotentials and rapid kinetics. The findings highlight that reversible oxygen redox is closely tied to the structural rigidity of the P2 phase and the stability provided by large dopants that prevent oxidized oxygen ions from interacting. Further developments of electrolytes are undoubtedly necessary to achieve long-term cycling at these high voltages. Nonetheless, by providing a clear pathway to the rational design and control of oxygen redox through synergistic doping and phase engineering, our work paves the way for the development of high-performance sodium-ion batteries with higher energy density.

Supporting Information. Experimental methods and supporting data (TGA, XANES spectra, pair distribution functions from EXAFS, wavelet transform EXAFS, RIXS maps, tables with structural information extracted from both XRD and FT-EXAFS), and further structural discussion.

Acknowledgements:

This work was funded by the Natural Sciences and Engineering Research Council of Canada under the auspices of a Discovery grant and a research contract with Umicore. We are grateful to Pierre-Etienne Cabelguen and the Umicore team for useful discussions regarding the RIXS data. Part of the research described in this paper was performed using the HXMA beamline at the Canadian Light Source, a national research facility of the University of Saskatchewan, which is supported by the Canada Foundation for Innovation (CFI), the Natural Sciences and Engineering Research Council (NSERC), the National Research Council (NRC), the Canadian Institutes of Health Research (CIHR), the Government of Saskatchewan, and the University of Saskatchewan. We acknowledge use of the Stanford Synchrotron Radiation Lightsource, SLAC National Accelerator Laboratory, is supported by the U.S. Department of Energy, Office of Science, Office of Basic Energy Sciences under Contract No. DE-AC02-76SF00515. SJL acknowledges the Quantum

Sensors Group at NIST-Boulder for their contributions to the development and support of the TES spectrometer at SSRL.

Reference:

(1) Zhang, C.; Wei, Y.-L.; Cao, P.-F.; Lin, M.-C. Energy Storage System: Current Studies on Batteries and Power Condition System. *Renewable and Sustainable Energy Reviews* **2018**, *82*, 3091–3106. https://doi.org/10.1016/j.rser.2017.10.030.
(2) Chayambuka, K.; Mulder, G.; Danilov, D. L.; Notten, P. H. L. From Li-Ion Batteries toward Na-Ion Chemistries: Challenges and Opportunities. *Advanced Energy Materials* **2020**, *10* (38), 2001310. https://doi.org/10.1002/aenm.202001310.
(3) Goodenough, J. B.; Park, K.-S. The Li-Ion Rechargeable Battery: A Perspective. *J. Am. Chem. Soc.* **2013**, *135* (4), 1167–1176. https://doi.org/10.1021/ja3091438.
(4) Goodenough, J. B.; Kim, Y. Challenges for Rechargeable Li Batteries. *Chem. Mater.* **2010**, *22* (3), 587–603. https://doi.org/10.1021/cm901452z.
(5) Wang, L.; Lu, Y.; Liu, J.; Xu, M.; Cheng, J.; Zhang, D.; Goodenough, J. B. A Superior Low-Cost Cathode for a Na-Ion Battery. *Angewandte Chemie International Edition* **2013**, *52* (7), 1964–1967. https://doi.org/10.1002/anie.201206854.
(6) Hwang, J.-Y.; Myung, S.-T.; Sun, Y.-K. Sodium-Ion Batteries: Present and Future. *Chemical Society Reviews* **2017**, *46* (12), 3529–3614. https://doi.org/10.1039/C6CS00776G.
(7) Jia, S.; Kumakura, S.; McCalla, E. Unravelling Air/Moisture Stability of Cathode Materials in Sodium Ion Batteries: Characterization, Rational Design, and Perspectives. *Energy & Environmental Science* **2024**, *17* (13), 4343–4389. https://doi.org/10.1039/D4EE00796D.
(8) Wang, M.; Wang, Q.; Ding, X.; Wang, Y.; Xin, Y.; Singh, P.; Wu, F.; Gao, H. The Prospect and Challenges of Sodium-Ion Batteries for Low-Temperature Conditions. *Interdisciplinary Materials* **2022**, *1* (3), 373–395. https://doi.org/10.1002/idm2.12040.
(9) Jia, S.; Counsell, J.; Adamič, M.; Jonderian, A.; McCalla, E. High-Throughput Design of Na–Fe–Mn–O Cathodes for Na-Ion Batteries. *Journal of Materials Chemistry A* **2022**, *10* (1), 251–265. https://doi.org/10.1039/D1TA07940A.
(10) Voronina, N.; Myung, S.-T. Recent Advances in Electrode Materials with Anion Redox Chemistry for Sodium-Ion Batteries. *Energy Material Advances* **2021**, *2021*. https://doi.org/10.34133/2021/9819521.
(11) Kim, D.; Cho, M.; Cho, K. Rational Design of Na(Li1/3Mn2/3)O2 Operated by Anionic Redox Reactions for Advanced Sodium-Ion Batteries. *Advanced Materials* **2017**, *29* (33), 1701788. https://doi.org/10.1002/adma.201701788.
(12) Perez, A. J.; Batuk, D.; Saubanère, M.; Rousse, G.; Foix, D.; McCalla, E.; Berg, E. J.; Dugas, R.; H. W. van den Bos, K.; Doublet, M.-L.; Gonbeau, D.; Abakumov, A. M.; Van Tendeloo, G.; Tarascon, J.-M. Strong Oxygen Participation in the Redox Governing the Structural and Electrochemical Properties of Na-Rich Layered Oxide Na2IrO3. *Chem. Mater.* **2016**, *28* (22), 8278–8288. https://doi.org/10.1021/acs.chemmater.6b03338.
(13) Mortemard de Boisse, B.; Liu, G.; Ma, J.; Nishimura, S.; Chung, S.-C.; Kiuchi, H.; Harada, Y.; Kikkawa, J.; Kobayashi, Y.; Okubo, M.; Yamada, A. Intermediate Honeycomb Ordering to Trigger Oxygen Redox Chemistry in Layered Battery Electrode. *Nat Commun* **2016**, *7* (1), 11397. https://doi.org/10.1038/ncomms11397.

(14) Xu, H.; Guo, S.; Zhou, H. Review on Anionic Redox in Sodium-Ion Batteries. *J. Mater. Chem. A* **2019**, *7* (41), 23662–23678. https://doi.org/10.1039/C9TA06389G.
(15) Cao, X.; Qiao, Y.; Jia, M.; He, P.; Zhou, H. Ion-Exchange: A Promising Strategy to Design Li-Rich and Li-Excess Layered Cathode Materials for Li-Ion Batteries. *Advanced Energy Materials* **2022**, *12* (4), 2003972. https://doi.org/10.1002/aenm.202003972.
(16) McCalla, E.; Jia, S. Topology to Improve Battery Technology. *Nat Sustain* **2022**, *5* (3), 181–182. https://doi.org/10.1038/s41893-021-00822-3.
(17) Jia, X.-B.; Wang, J.; Liu, Y.-F.; Zhu, Y.-F.; Li, J.-Y.; Li, Y.-J.; Chou, S.-L.; Xiao, Y. Facilitating Layered Oxide Cathodes Based on Orbital Hybridization for Sodium-Ion Batteries: Marvelous Air Stability, Controllable High Voltage, and Anion Redox Chemistry. *Advanced Materials* **2024**, *36* (15), 2307938. https://doi.org/10.1002/adma.202307938.
(18) Risthaus, T.; Zhou, D.; Cao, X.; He, X.; Qiu, B.; Wang, J.; Zhang, L.; Liu, Z.; Paillard, E.; Schumacher, G.; Winter, M.; Li, J. A High-Capacity P2 Na2/3Ni1/3Mn2/3O2 Cathode Material for Sodium Ion Batteries with Oxygen Activity. *Journal of Power Sources* **2018**, *395*, 16–24. https://doi.org/10.1016/j.jpowsour.2018.05.026.
(19) Yang, F.; Feng, X.; Liu, Y.-S.; Kao, L. C.; Glans, P.-A.; Yang, W.; Guo, J. In Situ/Operando (Soft) X-Ray Spectroscopy Study of Beyond Lithium-Ion Batteries. *ENERGY & ENVIRONMENTAL MATERIALS* **2021**, *4* (2), 139–157. https://doi.org/10.1002/eem2.12172.
(20) Cheng, C.; Zhuo, Z.; Chen, S.; Zhou, X.; Yuan, C.; Zeng, P.; Guo, J.; Zhang, L. Cationic and Anionic Redox of Battery Cathodes Investigated by Advanced Synchrotron-Based Mapping of Resonant Inelastic X-Ray Scattering. *Advanced Functional Materials* **2024**, *34* (39), 2403442. https://doi.org/10.1002/adfm.202403442.
(21) Jia, S.; Yao, E.; Peng, R.; Jonderian, A.; Abdolhosseini, M.; McCalla, E. Chemical Speed Dating: The Impact of 52 Dopants in Na–Mn–O Cathodes. *Chem. Mater.* **2022**, *34* (24), 11047–11061. https://doi.org/10.1021/acs.chemmater.2c03110.
(22) Jia, S.; Abdolhosseini, M.; Liu, C.; Jonderian, A.; Li, Y.; Kwak, H.; Kumakura, S.; Sieffert, J. M.; Eisnor, M.; McCalla, E. Stabilization of Na-Ion Cathode Surfaces: Combinatorial Experiments with Insights from Machine Learning Models. *Advanced Energy and Sustainability Research* **2024**, *5* (9), 2400051. https://doi.org/10.1002/aesr.202400051.
(23) Jonderian, A.; Jia, S.; Yoon, G.; Cozea, V. T.; Galabi, N. Z.; Ma, S. B.; McCalla, E. Accelerated Development of High Voltage Li-Ion Cathodes. *Advanced Energy Materials* **2022**, *12* (40), 2201704. https://doi.org/10.1002/aenm.202201704.
(24) Johari, N. S. M.; Jonderian, A.; Jia, S.; Cozea, V.; Yao, E.; Adnan, S. B. R. S.; Ahmad, N.; McCalla, E. High-Throughput Development of Na2ZnSiO4-Based Hybrid Electrolytes for Sodium-Ion Batteries. *Journal of Power Sources* **2022**, *541*, 231706. https://doi.org/10.1016/j.jpowsour.2022.231706.
(25) McCalla, E. Braving the Elements: Learning from 60+ Dopants in Battery Materials. *J. Phys. Chem. C* **2024**, *128* (40), 16831–16843. https://doi.org/10.1021/acs.jpcc.4c04870.
(26) House, R. A.; Rees, G. J.; McColl, K.; Marie, J.-J.; Garcia-Fernandez, M.; Nag, A.; Zhou, K.-J.; Cassidy, S.; Morgan, B. J.; Saiful Islam, M.; Bruce, P. G. Delocalized Electron Holes on Oxygen in a Battery Cathode. *Nat Energy* **2023**, *8* (4), 351–360. https://doi.org/10.1038/s41560-023-01211-0.
(27) Gent, W. E.; Lim, K.; Liang, Y.; Li, Q.; Barnes, T.; Ahn, S.-J.; Stone, K. H.; McIntire, M.; Hong, J.; Song, J. H.; Li, Y.; Mehta, A.; Ermon, S.; Tyliszczak, T.; Kilcoyne, D.; Vine, D.; Park, J.-H.; Doo, S.-K.; Toney, M. F.; Yang, W.; Prendergast, D.; Chueh, W. C. Coupling

between Oxygen Redox and Cation Migration Explains Unusual Electrochemistry in Lithium-Rich Layered Oxides. *Nat Commun* **2017**, *8* (1), 2091. https://doi.org/10.1038/s41467-017-02041-x.
(28) Hebert, A.; Galabi, N. Z.; Michael Sieffert, J.; Blangero, M.; McCalla, E. Elucidating the Impact of Metal Doping in Li 1.15 (Ni 0.35 Mn 0.65) 0.85 O 2 Cathodes Using High-Throughput Experiments and Machine Learning. *EES Batteries* **2025**. https://doi.org/10.1039/D4EB00016A.
(29) Li, Y.; Yang, Z.; Xu, S.; Mu, L.; Gu, L.; Hu, Y.-S.; Li, H.; Chen, L. Air-Stable Copper-Based P2-Na7/9Cu2/9Fe1/9Mn2/3O2 as a New Positive Electrode Material for Sodium-Ion Batteries. *Advanced Science* **2015**, *2* (6), 1500031. https://doi.org/10.1002/advs.201500031.
(30) Mason, C. W.; Lange, F.; Saravanan, K.; Lin, F.; Nordlund, D. Beyond Divalent Copper: A Redox Couple for Sodium Ion Battery Cathode Materials. *ECS Electrochem. Lett.* **2015**, *4* (5), A41. https://doi.org/10.1149/2.0041505eel.
(31) Wang, L.; Sun, Y.-G.; Hu, L.-L.; Piao, J.-Y.; Guo, J.; Manthiram, A.; Ma, J.; Cao, A.-M. Copper-Substituted Na 0.67 Ni 0.3−x Cu x Mn 0.7 O 2 Cathode Materials for Sodium-Ion Batteries with Suppressed P2–O2 Phase Transition. *Journal of Materials Chemistry A* **2017**, *5* (18), 8752–8761. https://doi.org/10.1039/C7TA00880E.
(32) Wang, X.; Yin, L.; Ronne, A.; Zhang, Y.; Hu, Z.; Tan, S.; Wang, Q.; Song, B.; Li, M.; Rong, X.; Lapidus, S.; Yang, S.; Hu, E.; Liu, J. Stabilizing Lattice Oxygen Redox in Layered Sodium Transition Metal Oxide through Spin Singlet State. *Nat Commun* **2023**, *14* (1), 7665. https://doi.org/10.1038/s41467-023-43031-6.
(33) Yang, W.; Devereaux, T. P. Anionic and Cationic Redox and Interfaces in Batteries: Advances from Soft X-Ray Absorption Spectroscopy to Resonant Inelastic Scattering. *Journal of Power Sources* **2018**, *389*, 188–197. https://doi.org/10.1016/j.jpowsour.2018.04.018.
(34) Frati, F.; Hunault, M. O. J. Y.; de Groot, F. M. F. Oxygen K-Edge X-Ray Absorption Spectra. *Chem. Rev.* **2020**, *120* (9), 4056–4110. https://doi.org/10.1021/acs.chemrev.9b00439.
(35) Wang, Z.; Alrehaily, L.; Joseph, J.; Wren, J. C.; Wang, J.; Sham, T.-K. Scanning Transmission X-Ray Microscopy Studies of Chromium Hydroxide Hollow Spheres and Nanoparticles Formed by Gamma Radiation. *Can. J. Chem.* **2017**, *95* (11), 1146–1150. https://doi.org/10.1139/cjc-2017-0142.
(36) Marie, J.-J.; Jenkins, M.; Chen, J.; Rees, G.; Cellorio, V.; Choi, J.; Agrestini, S.; Garcia-Fernandez, M.; Zhou, K.-J.; House, R. A.; Bruce, P. G. Reversible Electron–Holes on O in P2-Type Na0.67Li0.1Ni0.3Mn0.6O2. *Advanced Energy Materials* **2024**, *14* (41), 2401935. https://doi.org/10.1002/aenm.202401935.
(37) Xu, J.; Sun, M.; Qiao, R.; Renfrew, S. E.; Ma, L.; Wu, T.; Hwang, S.; Nordlund, D.; Su, D.; Amine, K.; Lu, J.; McCloskey, B. D.; Yang, W.; Tong, W. Elucidating Anionic Oxygen Activity in Lithium-Rich Layered Oxides. *Nat Commun* **2018**, *9* (1), 947. https://doi.org/10.1038/s41467-018-03403-9.
(38) Zhuo, Z.; Dai, K.; Qiao, R.; Wang, R.; Wu, J.; Liu, Y.; Peng, J.; Chen, L.; Chuang, Y.; Pan, F.; Shen, Z.; Liu, G.; Li, H.; Devereaux, T. P.; Yang, W. Cycling Mechanism of Li2MnO3: Li–CO2 Batteries and Commonality on Oxygen Redox in Cathode Materials. *Joule* **2021**, *5* (4), 975–997. https://doi.org/10.1016/j.joule.2021.02.004.
(39) Zhuo, Z.; Liu, Y.; Guo, J.; Chuang, Y.; Pan, F.; Yang, W. Full Energy Range Resonant Inelastic X-Ray Scattering of O2 and CO2: Direct Comparison with Oxygen Redox State in

Batteries. *J. Phys. Chem. Lett.* **2020**, *11* (7), 2618–2623. https://doi.org/10.1021/acs.jpclett.0c00423.
(40) Mortemard de Boisse, B.; Nishimura, S.; Watanabe, E.; Lander, L.; Tsuchimoto, A.; Kikkawa, J.; Kobayashi, E.; Asakura, D.; Okubo, M.; Yamada, A. Highly Reversible Oxygen-Redox Chemistry at 4.1 V in Na4/7−[□1/7Mn6/7]O2 (□: Mn Vacancy). *Advanced Energy Materials* **2018**, *8* (20), 1800409. https://doi.org/10.1002/aenm.201800409.
(41) Chen, D.; Wu, J.; Papp, J. K.; McCloskey, B. D.; Yang, W.; Chen, G. Role of Redox-Inactive Transition-Metals in the Behavior of Cation-Disordered Rocksalt Cathodes. *Small* **2020**, *16* (22), 2000656. https://doi.org/10.1002/smll.202000656.
(42) Dai, K.; Wu, J.; Zhuo, Z.; Li, Q.; Sallis, S.; Mao, J.; Ai, G.; Sun, C.; Li, Z.; Gent, W. E.; Chueh, W. C.; Chuang, Y.; Zeng, R.; Shen, Z.; Pan, F.; Yan, S.; Piper, L. F. J.; Hussain, Z.; Liu, G.; Yang, W. High Reversibility of Lattice Oxygen Redox Quantified by Direct Bulk Probes of Both Anionic and Cationic Redox Reactions. *Joule* **2019**, *3* (2), 518–541. https://doi.org/10.1016/j.joule.2018.11.014.
(43) Abate, I. I.; Pemmaraju, C. D.; Kim, S. Y.; Hsu, K. H.; Sainio, S.; Moritz, B.; Vinson, J.; Toney, M. F.; Yang, W.; Gent, W. E.; Devereaux, T. P.; Nazar, L. F.; Chueh, W. C. Coulombically-Stabilized Oxygen Hole Polarons Enable Fully Reversible Oxygen Redox. *Energy Environ. Sci.* **2021**, *14* (9), 4858–4867. https://doi.org/10.1039/D1EE01037A.
(44) Luo, K.; Roberts, M. R.; Hao, R.; Guerrini, N.; Pickup, D. M.; Liu, Y.-S.; Edström, K.; Guo, J.; Chadwick, A. V.; Duda, L. C.; Bruce, P. G. Charge-Compensation in 3d-Transition-Metal-Oxide Intercalation Cathodes through the Generation of Localized Electron Holes on Oxygen. *Nature Chem* **2016**, *8* (7), 684–691. https://doi.org/10.1038/nchem.2471.
(45) Song, B.; Tang, M.; Hu, E.; Borkiewicz, O. J.; Wiaderek, K. M.; Zhang, Y.; Phillip, N. D.; Liu, X.; Shadike, Z.; Li, C.; Song, L.; Hu, Y.-Y.; Chi, M.; Veith, G. M.; Yang, X.-Q.; Liu, J.; Nanda, J.; Page, K.; Huq, A. Understanding the Low-Voltage Hysteresis of Anionic Redox in Na2Mn3O7. *Chem. Mater.* **2019**, *31* (10), 3756–3765. https://doi.org/10.1021/acs.chemmater.9b00772.
(46) Boivin, E.; House, R. A.; Marie, J.-J.; Bruce, P. G. Controlling Iron Versus Oxygen Redox in the Layered Cathode Na0.67Fe0.5Mn0.5O2: Mitigating Voltage and Capacity Fade by Mg Substitution. *Advanced Energy Materials* **2022**, *12* (30), 2200702. https://doi.org/10.1002/aenm.202200702.
(47) Xia, Z.; Zhang, H.; Shen, K.; Qu, Y.; Jiang, Z. Wavelet Analysis of Extended X-Ray Absorption Fine Structure Data: Theory, Application. *Physica B: Condensed Matter* **2018**, *542*, 12–19. https://doi.org/10.1016/j.physb.2018.04.039.
(48) Timoshenko, J.; Kuzmin, A. Wavelet Data Analysis of EXAFS Spectra. *Computer Physics Communications* **2009**, *180* (6), 920–925. https://doi.org/10.1016/j.cpc.2008.12.020.
(49) Talaie, E.; Duffort, V.; L. Smith, H.; Fultz, B.; F. Nazar, L. Structure of the High Voltage Phase of Layered P2-Na 2/3−z [Mn 1/2 Fe 1/2]O 2 and the Positive Effect of Ni Substitution on Its Stability. *Energy & Environmental Science* **2015**, *8* (8), 2512–2523. https://doi.org/10.1039/C5EE01365H.

Table of contents graphic